

# Analysis of Stress and Strain Around Orthodontically Loaded Implants: An Animal Study

Paolo M. Cattaneo, MSc, PhD<sup>1</sup>/Michel Dalstra, MSc, PhD<sup>2</sup>/Birte Melsen, DDS, Dr Odont<sup>3</sup>

**Purpose:** The aim of this study was to describe the stress and strain fields around orthodontically loaded dental implants using the finite element method and to evaluate the relationship between the generated strain and the biologic reaction expressed through histomorphometric parameters. Finally, this study aimed to evaluate the interaction between the orthodontic loading and the deformation generated by normal occlusal function. **Materials and Methods:** Sixteen titanium dental implants were inserted in extraction sockets after the removal of the second premolars and first molars of 4 adult *Macaca fascicularis* monkeys. After 17 weeks of healing, the implants were loaded by a pair of Sentaloy springs (50 cN) for 16 weeks. After sacrifice, tissue blocks including the implants and surrounding bone were excised. Five tissue blocks were scanned with a synchrotron radiation-based microtomography ( $\mu$ CT) scanner and sample-specific finite element models were generated. Subsequently all samples were prepared for histomorphometric analysis. **Results:** All implants were osseointegrated, although the surrounding alveolar bone differed from sample to sample. As a consequence the finite element analyses showed that the stresses and strains in the peri-implant alveolar bone greatly varied among the samples. A high level of remodeling activity was found close to the implants. **Discussion:** Individual differences between the receptors (in this case, the monkeys) have a large effect on both the biologic and morphologic parameters. These variations were indeed found to have a substantial impact on the (re)modeling dynamics and the load transfer mechanisms around the implants. **Conclusions:** By integrating different analysis techniques to evaluate bone (re)modeling around orthodontically loaded implants, this study has demonstrated the complexity and case-specific character of alveolar adaptation to orthodontic loading. Furthermore, stresses generated by combined functional and orthodontic forces should not be neglected. (More than 50 references) INT J ORAL MAXILLOFAC IMPLANTS 2007;22:213–225

**Key words:** biomechanics, dental implants, finite element analysis, histomorphometry, osseointegration

Over the past 30 years, endosseous dental implantation has been established as a valid method to restore oral function in totally or partially edentulous patients.<sup>1–4</sup> To describe the attachment of the adjacent bone to the surface of the titanium implant, the term *osseointegration* was introduced.<sup>5</sup> The definition of osseointegration is, however, far from universal. The dynamics of bone as a tissue must be taken into consideration. As a consequence of ongoing

process of bone remodeling, osseointegration cannot be considered a static index. It is directly related to the dynamic nature of bone; thus, the implant-bone interface can change over time. Additional information that should be implicit in the term *osseointegration* is the amount of osseous contact that is necessary for an implant to be considered osseointegrated. It has been demonstrated that an implant can be stable with only 10% of its surface in contact with bone<sup>6</sup> and that even as little as 5% bone-implant contact is sufficient to guarantee stability in case of orthodontic loading.<sup>7</sup> Yet no minimum values have been defined. The type of bone in contact with the implants is also expected to play a major role in the interface strength.<sup>8,9</sup>

The mechanical retention of implants in the recipient sites can be explained by 2 different mechanisms acting simultaneously, macroretention and microretention.<sup>3,4</sup> Macroretention is the mechanical retention and is provided by the geometrical shape

<sup>1</sup>Assistant Professor, Department of Orthodontics, School of Dentistry, Aarhus University, Aarhus, Denmark.

<sup>2</sup>Associate Professor, Department of Orthodontics, School of Dentistry, Aarhus University, Aarhus, Denmark.

<sup>3</sup>Professor and Chair, Department of Orthodontics, School of Dentistry, Aarhus University, Aarhus, Denmark.

**Correspondence to:** Dr Paolo M. Cattaneo, Department of Orthodontics, School of Dentistry, University of Aarhus, Vennelyst Boulevard 9, 8000 Aarhus C, Denmark. Fax +45 86192752. E-mail: pcattaneo@odont.au.dk

of implant. Threads, undercuts, ridges, and holes can provide better fixation through mechanical macrointerlock. Microretention is provided by the physical characteristics of the surface. It has been reported that implant surfaces that present a finer scale of surface roughness, such as plasma-sprayed surfaces and sand-blasted surfaces, allow bone ingrowth into surface microirregularities. Thus, these surfaces provide better fixation than smooth titanium implants. A chemical bond between bone and the titanium plates has been hypothesized; however, the mechanism leading to formation of the chemical bone-implant bond has not been elucidated.<sup>10</sup>

### Bone Remodeling Around Loaded Implants

The remodeling duration ( $\sigma$ ) for the cortical bone in various species has been reported to be about 6 weeks in rabbits, 12 weeks in dogs, and 16 weeks in humans, while for monkeys an estimate of 14 weeks has been proposed.<sup>8,11-14</sup> A more detailed study performed on *Macaca fascicularis* monkeys reported that the activation frequency in trabecular bone was  $1.43 \pm 0.37$  per year; the resorption period, including the reversal period,  $27 \pm 10$  days; and the formation period,  $42 \pm 10$  days. The bone volume fraction (ie, the relative fraction of bone volume) was  $26.4\% \pm 1.3\%$ .<sup>15</sup>

Many in vivo implant studies have attempted to provide indexes to relate implant stability to the type, quality, and amount of bone surrounding endosseous implants. In a study performed on rabbits, dogs, monkeys, and humans, it was found that the amount of bone in the region adjacent to the implants (~1 mm) in all species was 1.5 to 2-fold greater than in regions distant from the implant surface. The remodeling rate was also found to be elevated by 3 to 4 times in rabbits, dogs, and monkeys, while in humans it was increased by about 9-fold.<sup>8</sup> In spite of a normal remodeling rate of 3% to 8% per year<sup>16</sup> for human cortical bone in adults, the remodeling rate around oral implants has been found to be 30% per year.<sup>17</sup> Indeed, both the increased bone volume density and the increased remodeling rate in the areas close to implants appear to reflect a steady-state condition, as a similar situation was indeed observed in bone around implants implanted up to 5 years. These phenomena might be key factors that could assure long-term stability to endosseous implants.<sup>8,18,19</sup>

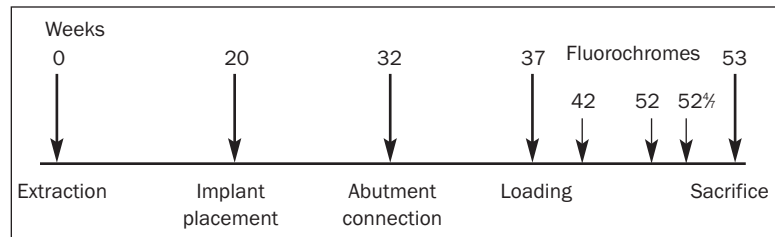
A possible explanation of the high remodeling rate subsequent to implant placement has been that it is an attempt to limit the microdamage accumulation generated by fatigue.<sup>20</sup> A relationship between loading of the implant and the tissue reaction adjacent to the implant has been the subject of several studies. However, the loading conditions have been

described only based on a hypothetical model and thus expressed only as an approximation of real loading. The tissue reaction has been described but not directly related to true strain values, as only the total load rather than the load distribution has been reported. The interrelationship between the actual stress and strain levels around a loaded implant, the modeling/remodeling rate, and the resulting change in bone volume fraction in the corresponding areas has not yet been fully elucidated.

Finite element (FE) models have been developed in the past to quantify the stress and strain fields in the bony tissues around dental implants. However, the aims of the different studies were not unique. Some of the studies were focused on the strain and stress levels in the bone surrounding the implants when chewing forces were applied to the implants,<sup>21-26</sup> while in other studies the aim was to determine the strain and stress patterns when the implants were loaded with continuous orthodontic forces.<sup>18,27,28</sup> In the aforementioned studies, the main problems in modeling the implant-bone complex in the dental area arose when trying to describe precisely the geometry of the anatomic parts, the inner morphology and material properties of bony tissues, the true 3D loading and boundary conditions, and the nature of the implant-bony tissue interfaces.<sup>29</sup> To deal with these difficulties, various levels of simplification have been introduced. For example, different assumptions have been made with respect to the implant-bone interface. It has been considered either fully bonded or nonbonded. The bone has been modeled as either homogeneous or nonhomogeneous tissue and as either isotropic or anisotropic material. Its behavior has been modeled as linear elastic or nonlinear behavior. Moreover, in most instances, the implant was modeled as standing in an arbitrarily defined block of bone; only rarely has a model included placement in a realistically modeled part of the jaw. These substantial differences suggest caution in interpreting and comparing the results of various studies.

Based on these premises, the aims of the present study were:

1. To describe the stress distribution around dental implants loaded with orthodontic forces
2. To estimate the resulting strain on the basis of FE analyses
3. To evaluate the relationship between the generated strain and the biologic reaction reflected histomorphometrically
4. To evaluate the interaction between the orthodontic loading and the deformation generated by normal occlusal function

**Fig 1** Timeline of the experiment.

## MATERIALS AND METHODS

Four adult male *M fascicularis* monkeys 6 to 7 years of age with a mean body weight of  $6.5 \pm 0.5$  kg were included in this study. They were purchased from the National Bacteriological Laboratory, Stockholm, Sweden, and were acclimatized for about a year and a half. The monkeys were single-caged and fed following a standard diet composed mainly of vegetables and fruit plus a smaller amount of proteins. The diet was kept the same during throughout the experiment. The timeline of the animal experiment is depicted in Fig 1.

The animals were anesthetized, and all second premolars and first molars were extracted. Following 20 weeks of uneventful healing, radiographs and impressions of the extraction sites were obtained. Subsequently, the healed alveolar process was exposed by means of a mucoperiosteal flap, using a midcrestal incision. Following the manufacturer's guidelines, 1 conical screw-shaped implant (Exacta; Biagini Medical Devices, La Spezia, Italy) was placed in each extraction site ( $n = 16$ ). The implants were fitted with a closing screw, and the wound was sutured. The implants, which had a maximum cervical diameter of 3.3 mm and a length of 7 mm, were made of commercially pure titanium and had a sand-blasted surface with a 1.5-mm polished neck. The implants were allowed to heal submerged for 17 weeks. Five weeks before loading, a specially manufactured abutment was fitted to the implants. Fourteen implants were loaded with 50 cN. The load was generated by 2 superelastic Sentalloy springs (Dentsply/GAC International, Bohemia, NY), tested to generate a force of 25 cN each. One spring was attached to the buccal aspect of the abutment and 1 to the lingual aspect. Both springs extended toward the ipsilateral canine in the maxilla and toward the molars in the mandible. The loading period was 16 weeks. The remaining 2 implants, 1 maxillary and 1 mandibular, were left unloaded and served as controls.

To determine that loading exerted on the implants was continuous at the intended level and in a healthy environment, all monkeys were submitted to an oral hygiene program twice a week. During oral hygiene examinations, the stability of the implants was verified,

**Table 1** Sequence, Timing, and Dosage of Intravital Bone-Labeling Fluorochromes

Label	Dosage (mg/kg)	Time of administration
Tetracycline	20	5 weeks after loading
Xylenol orange	60	1 week before sacrifice
Calcein	10	3 days before sacrifice

the coil springs were checked, and if necessary, replaced, and all teeth and the interfaces between implants and gingival soft tissues were brushed with a soft-bristle toothbrush dipped in 0.2% chlorhexidine.

In order to analyze the dynamics of the bone surrounding the implants, intravital bone-labeling fluorochromes were administered intravenously. Tetracycline (20 mg/kg), xylenol orange (60 mg/kg), and calcein (10 mg/kg) labels were used as bone markers following the timing sequence reported in Table 1. Following a 16-week loading period, the animals were euthanized by an overdose of pentobarbital (100 mg/mL). The maxilla and mandible were removed, and tissue blocks including each implant and the surrounding bone were excised and processed for the generation of undecalcified sections. The samples were organized as shown in Table 2.

### Histologic Preparation and Analysis

Sections perpendicular to the long axis of the implant were produced from each block using a Leiden microtome cutting system, Exakt Apparatebau, Leiden, The Netherlands). The section thickness was 40  $\mu$ m, and the distance between sections was about 420  $\mu$ m. On average, 20 sections were obtained from each block. The sections were alternatively stained with toluidine blue or left unstained for the analysis of the fluorochrome stains.

Two adjacent sections from 3 different levels were selected for histomorphometric analysis: 2 close to the gingival margin, 2 at the center, and 2 at the apical end of the implant. Starting from the implant apex, the 3 levels were respectively referred to as the "bottom," "center," and "top." The most apical layer (bottom) was identified as a section characterized by a distance of 20 to 1,380  $\mu$ m from the apex (Fig 2). The center layer was 1,840  $\mu$ m from the bottom layer, and the top layer

Table 2 Sample Names by Monkey		
Monkey	Jaw	Sample name
1	Right mandible	1-LR
	Left mandible	1-LL
	Right maxilla	1-UR
2	Left maxilla	1-UL
	Right mandible	2-LR
	Left mandible*	2-LL
	Right maxilla*	2-UR
3	Left maxilla	2-UL
	Right mandible	3-LR
	Left mandible	3-LL
	Right maxilla	3-UR
4	Left maxilla	3-UL
	Right mandible	4-LR
	Left mandible	4-LL
	Right maxilla	4-UR
	Left maxilla	4-UL

\*Control.

was 1,840  $\mu\text{m}$  from the center layer (Fig 2). Custom-made grids consisting of 3 concentric circles centered on the axis of the implant were mounted on all sections. The inner circle corresponded to the outer perimeter of the implant. Two lines at 90 degrees to one another intersected in the circle center. The circle and the lines defined 8 regions each, composing an area of 5.48  $\text{mm}^2$  (Fig 2). Only the regions in the direction of the line of the force (mesial-distal direction) were used. All histologic evaluations were performed with an Olympus BH-2 microscope (Olympus Danmark A/S, Ballerup, Denmark) equipped with a Zeiss II integrating reticle (Zeiss, Oberkochen, Germany) with equidistant parallel test lines and points, at a final magnification of  $\times 125$ , under both visible and ultraviolet epifluorescent light. The microscopic fields were repeatedly chosen inside each region while the orientation of the reticle was changed through random rotation.

Bone volume fraction (BV/TV) was evaluated in each region using the grid by a point-counting method. There were about 700 points within each region. BV/TV was calculated as a percentage of mineralized bone and osteoid to total tissue volume.<sup>30</sup>

The activity of the bone in the different regions around the implant was evaluated considering the

- Fractional resorption surface: Resorption lacunae were identified as scalloped defects on the bone surface, and the relative extension of resorption lacunae was expressed as a percentage of the total bone surface within each region.
- Fractional formation surface: The extent of the bone surface covered by osteoid was expressed as a percentage of the total bone surface within each region.

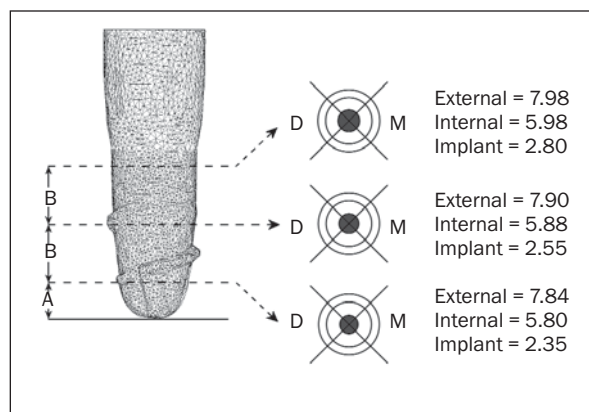


**Fig 2** Positions of the histologic sections relative to the implant and the diameters of the circular grids (D = distal, M = mesial). Units are given in mm.

- Fractional resting surface: The extent of surface without any ongoing remodeling was expressed as a percentage of the total bone surface.<sup>30</sup>

Bone remodeling dynamics were calculated as the relative extension of the mineralizing surface to bone surface (MS/BS) by classifying single- and double-labeled surfaces (sLS and dLS, respectively) as a percentage of the total bone surface<sup>13</sup>:

$$\text{MS/BS} = \frac{\text{sLS}/2 + \text{dLS}}{\text{BS}}$$

Finally, bone-implant contact (BIC) was estimated as the percentage of bone in contact with the implant surface using a star-shaped grid consisting of 16 lines passing through the implant center.

### Micro-CT Scanning

In order to describe inner and outer morphology of the samples, 5 3-dimensional (3D) blocks, 3 from maxillae and 2 from mandibles of different monkeys were scanned with a synchrotron radiation (SR) -based microcomputerized tomography ( $\mu\text{CT}$ ) scanner (beamline W2; DORIS, HASYLAB at DESY, Hamburg, Germany).<sup>31</sup> Scanning was performed using a monochromatic beam at an energy level of 50 keV. The reconstructions of the 3D datasets were made starting from the sinograms using a filtered back-projection algorithm. The datasets had a spatial resolution of 16  $\mu\text{m}$ .

### Generation of the FE Model

Based on the  $\mu$ CT datasets, 5 FE models were generated from the scanned tissue blocks. The segmentation of alveolar bone and the titanium implant was performed using 3D visualization software (Mimics 7.10; Materialise, Leuven, Belgium) by applying 2 different threshold levels. The segmented structures were modeled as different geometric entities using a surface triangularization technique and were subsequently stored in individual files using the stereo lithography (STL) file format and converted into the drawing exchange (DXF) file format. Finally, each single part was imported into the preprocessor of the FE code (COSMOS/M 2.9; Structural Research & Analysis Corporation, Los Angeles, CA). The automatic mesh generator of COSMOS/M was used to generate the final FE meshes of the parts; 4-node tetrahedral elements were produced. The different parts were meshed using mean element sizes that differed according to their geometrical dimensions. When meshing the areas close to the common boundary surfaces (ie, the surfaces between the implant and the alveolar bone), smaller mean element sizes were used, allowing for a more accurate description of the local geometry and providing better calculation of the stresses and strains. This procedure resulted in up to 1,022,271 tetrahedral elements with an average dimension of 0.175 mm; 183,884 nodes; and 551,514 degrees of freedom (Table 3).

The bone-implant interface was assumed to be bonded, and consequently, sliding at the interface was not incorporated into the FE model. To minimize the effects of the clamped edges, an elastic zone with a thickness of 0.5 mm was simulated mesially and apically with respect to the implant for the maxillary models and distally and coronally for mandibular models.

### Material Properties

Material property assignment was a semi-automated procedure. Each element representing bone was individually assigned a different Young's modulus based on the true morphology of the bone as obtained from the original CT scans using a slightly modified version of the procedure implemented by Cattaneo et al.<sup>32</sup> In IDL (Interactive Data Language; Research Systems, Boulder, CO) the CT datasets were converted into arrays containing the coordinates and corresponding grey values. A specific C-program was written to calculate the coordinates of the centroid of each element and, based on these coordinates, to retrieve the corresponding grey value from the array. Three threshold values were identified, each corresponding to the boundaries between bone marrow, bone, and implant. The retrieved grey value was converted into a

**Table 3** Description of the FE Models

Specimen	No. of elements	No. of nodes	df
1-LL	1,022,271	183,884	551,514
1-UL	875,052	157,427	472,281
3-LR	933,449	168,262	491,235
3-UL	674,589	121,963	365,889
4-UR	990,186	175,822	527,466

df = degrees of freedom.

stiffness value according to the thresholds. Thus, 3 different Young's moduli were considered to represent full cortical bone (17,500 MPa, Poisson's ratio of 0.3), mixed bone (ie, where the centroid lay on the border between bone and bone marrow; 5,000 MPa, Poisson's ratio of 0.3), and bone marrow (50 MPa, Poisson's ratio of 0.45), respectively (Fig 3).

The elements representing the implants were assigned a Young's modulus of 110,000 MPa and a Poisson's ratio of 0.3, while the material property of the 2 elastic zones was modeled with a Young's modulus of 600 MPa and a Poisson's ratio of 0.3.

### Loading and Boundary Conditions

For each model a load of 50 cN was distributed among the nodes in the same zone where the implants were loaded in vivo. The loading direction was chosen according to the extension of the spring attached to the teeth.

For the boundary conditions, movement was suppressed in all directions for the nodes situated on the bottom external edges of the elastic blocks, while movement was suppressed only along the direction of the loading force for all the nodes situated on the mesial and distal regions of the elastic bands.

In order to evaluate the impact of occlusion, a force of about 55 N at the canine/premolar region was applied to 1 of the FE models (sample 3-LR). This value was chosen by interpolating the data for a macaque chewing an apple.<sup>33</sup>

### Processing the Results

For the FE model the same regions determined for the histomorphometric analyses were identified around the implant. The thickness of the layers analyzed was set at 0.6 mm (0.3 mm on each side of the center of the corresponding histologic section) in order to have a physical volume in which the stress and strain fields could be calculated. Three different parameters were evaluated: (1) the Von Mises stress ( $\sigma_{VM}$ ); (2) the difference between the maximum and minimum principal strains, which was equal to the maximal shear strain; and (3) the equivalent (or effective) strain ( $\epsilon_{eq}$ ).

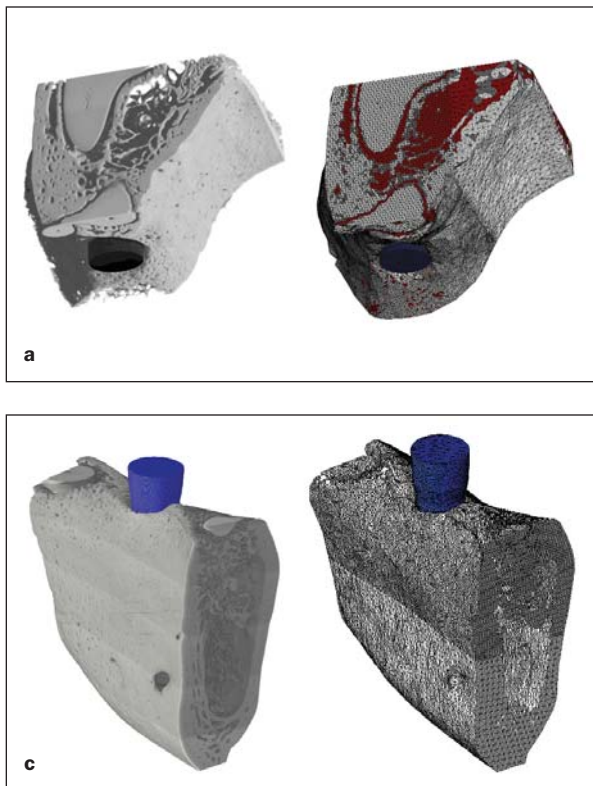
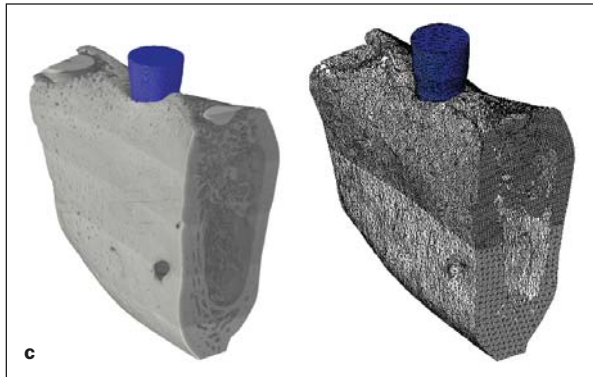


**Fig 3** 3D volume rendering of sample 4-UR obtained from  $\mu$ CT scanning (3a, left) and its corresponding FE model (3a, right). A single-slice scan of sample 1-LL (3b, left) and the corresponding section from the FE model (3b, right) are also presented. The  $\mu$ CT 3D rendering of sample 3-LR (3c, left) is presented with the corresponding FE where only the bone is depicted (3c, right).



## RESULTS

The histologic evaluation showed that resorption was significantly higher for the loaded group in comparison with the control group for all 3 levels. On the contrary, fractional resting surface was significantly higher for the control group. The remaining evaluations showed no statistically significant differences between the 2 groups.

A statistically significant difference in MS/BS was found between the 2 external regions only for the top layer. Moreover, the difference in the BV/TV was statistically significant between the internal and external regions on both sides of the implant in the top layer. A statistically significant difference in BV/TV was also found between the 2 outer regions for both the center and bottom layers, and between the 2 internal regions for the center layer.

The SR  $\mu$ CT-scanning technique is able to generate sharp and clear representations of the bone, even in close contact with the implant, thereby limiting the artifacts and the beam-hardening effects to almost nothing. The comparison of the SR  $\mu$ CT scans with the histologic sections revealed that the level of detail was similar whenever it was necessary to discriminate between bone and marrow, even in proximity to the implant surface (Fig 4). The scanning rendered it possible to determine the exact insertion

location of the implant and the morphology of the surrounding alveolar bone 3-dimensionally for each sample (Fig 5).

Based both on the qualitative evaluation of the 3D datasets and on the results from the BIC calculation (Table 4), it could be assumed that the implants were well osseointegrated, as new bone covered the endosseous surface of the implant almost completely. The 3D evaluation revealed that despite the use of a standard insertion procedure and implant location, the peri-implant alveolar bone varied from sample to sample with respect to both density and type (Fig 5).

As a consequence, the FE analyses show that the 5 implants, despite the fact that they were all loaded with forces of the same magnitude, were characterized by different types of displacement. Specifically, the center of rotation of sample 3-UL was located 0.7 mm more apically and more distally than the other 2 loaded implants placed in maxillary bone. The cervical end of sample 3-LR experienced less displacement than the cervical ends of the other samples (Fig 6).

The von Mises stresses in the alveolar bone (Fig 7) demonstrate that the cervical portion of the bone, characterized by cortical shell, is bearing most of the load. As a result of the pronounced tipping in case of samples 1-LL and 1-UL, the bone close to the apical tip of the implant was also loaded. Looking at the stress component parallel to the loading direction, it

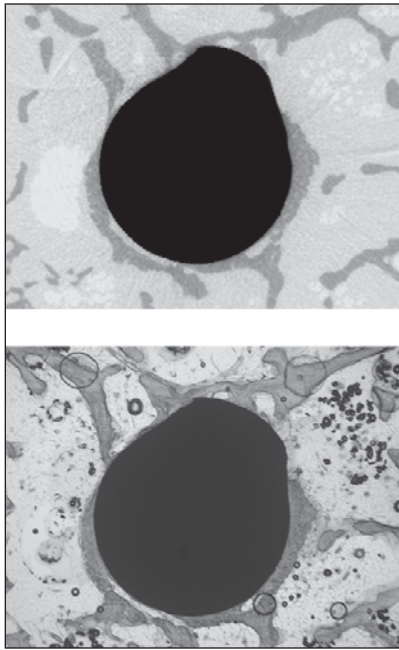


**Fig 4** Close-up images of the bone-implant interface obtained from  $\mu$ CT scanning (*top*) and conventional histology (*bottom*).

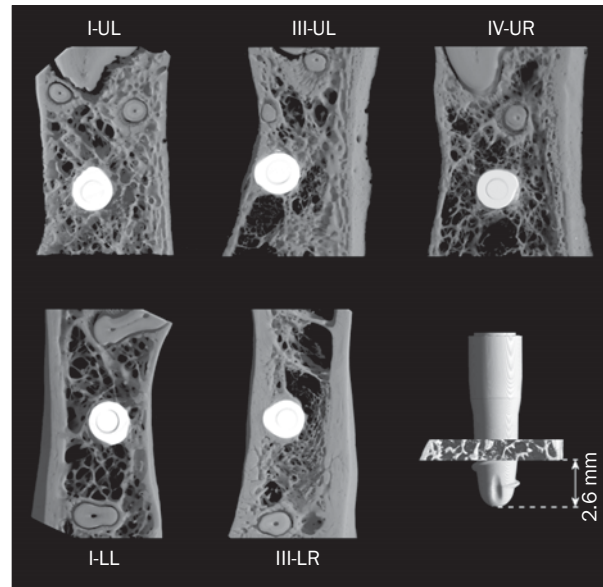


**Fig 5** Three-dimensional volume rendering of 1,440- $\mu$ m-thick sections of the 5 samples obtained from  $\mu$ CT scanning. All renderings were taken 2.6 mm from the tip of the implant. Note the different peri-implant bone morphology from sample to sample.

**Table 4** Percentage of BIC

Sample	BIC (%)	SD
1-LR	85.4	6.8
1-LL	81.8	9.3
1-UR	85.4	7.6
1-UL	81.3	6.6
2-LR	52.1	10.4
2-LL	54.5	23.4
2-UR	49.2	8.2
2-UL	64.4	11.8
3-LR	78.1	12.0
3-LL	72.4	11.4
3-UR	75.1	11.6
3-UL	75.5	10.0
4-LR	75.0	6.6
4-LL	74.5	23.6
4-UR	86.4	8.4
4-UL	79.2	7.0

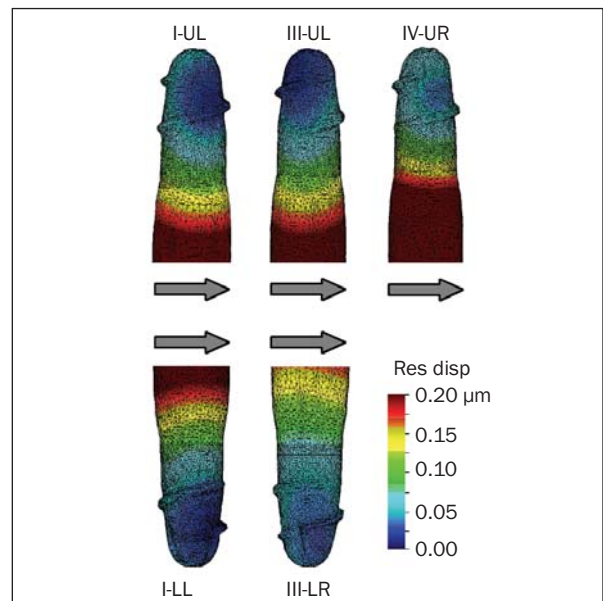


**Fig 6** Displacement in  $\mu$ m of the implant in the 5 different FE models when the orthodontic force was applied (top row, maxillary samples; bottom row, mandibular samples).

can be observed that in case of samples 3-LR and 3-UL, due to the insertion of the implants close to the buccal external surface of the alveolar bone (Fig 5), most of the load was transferred from the implant to the cervical and buccal cortices. Thus, the trabecular bone in proximity to the apex of the implant carried only a minimal part of the load (Fig 8). In the other samples, the bone surrounding the apex of the

implant (ie, trabecular bone) bore a more substantial part of the load (Fig 8). For the same reason, examination of the same sagittal sections reveals that degree of deformation of the peri-implant bone varied from sample to sample (Fig 9). The highest strain levels were found in the bone around implant 4-UR, while the bone close to the apex of implants 3-LR and 3-UL was subjected only to minimal deformation.

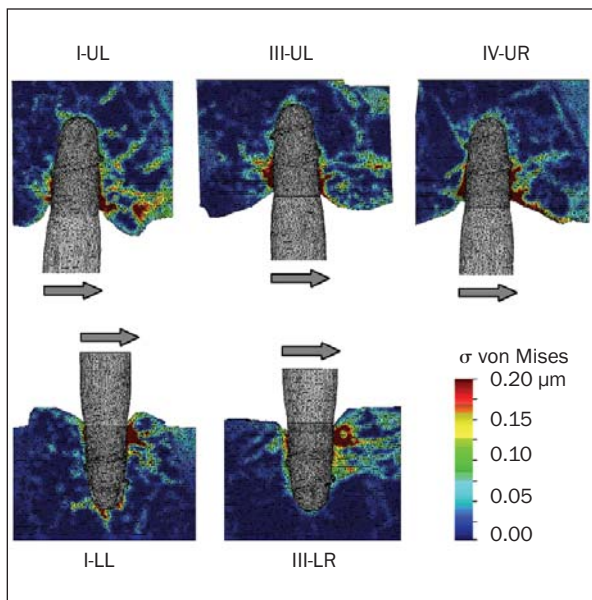


**Fig 7** Von Mises stress distribution in MPa in a sagittal cross section of the alveolar bone around the implants.

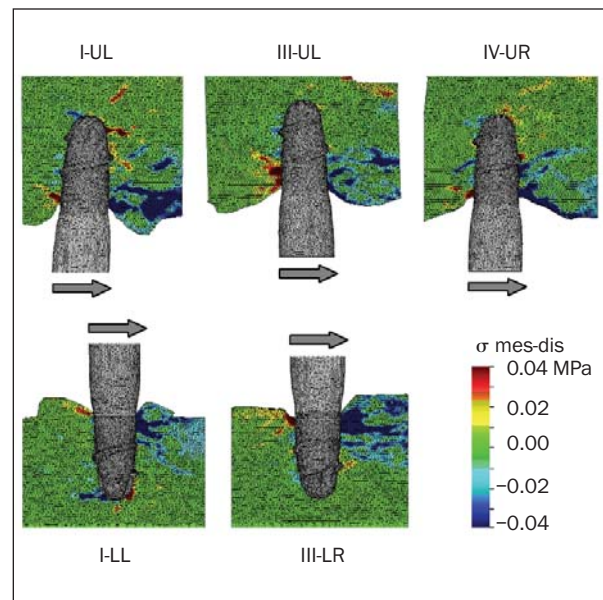


**Fig 8** Stress distribution in MPa in the direction of the load in a sagittal cross section of the alveolar bone around the implants. Blue denotes compressive stresses, red tensile.

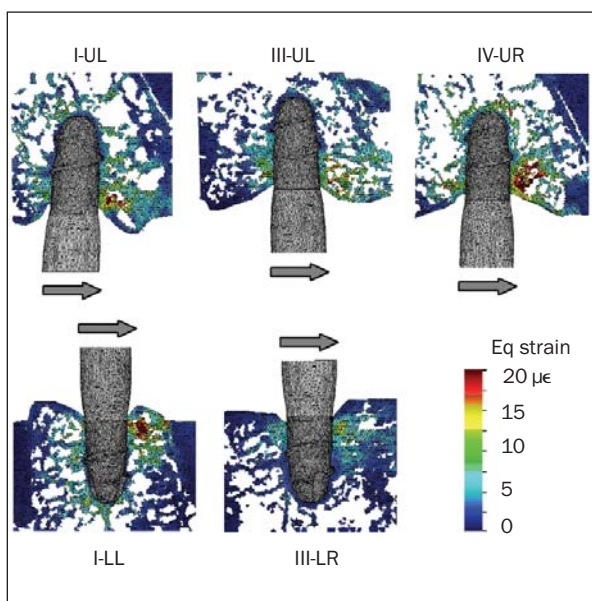


**Fig 9** Equivalent strain distribution in  $\mu\epsilon$  in a sagittal cross-section of the alveolar bone around the implants. Note the low strain values in the bone adjacent to the implants (lamina dura). The bone marrow elements were removed for intelligibility.

In all samples, the layer of bone close to the implant surface, also referred to as lamina dura, exhibited a low strain level (Fig 9).

The equivalent and maximal shear strains calculated in the areas corresponding to the regions selected for the histomorphometric evaluation are depicted in Fig 10. In the regions of the top layer the strain levels were similar for all 5 implants; they ranged from 8 to 14  $\mu\text{strain}$  in the inner regions and from 8 to 10  $\mu\text{strain}$  in the outer regions. In the center layer, the strains ranged from 3 to 6  $\mu\text{strain}$ , while in the bottom layer, the strains ranged from 2 to 5  $\mu\text{strain}$  and from 3 to 5  $\mu\text{strain}$  for the outer and the inner regions, respectively. Note that the strain levels were sample-dependent, as they were determined by the type and morphology of the alveolar bone where the implants were inserted.

In order to correlate the aforementioned strains with the morphometric and dynamic parameters measured in the corresponding regions, a regression analysis was performed for each sample individually. A statistically significant correlation between strain and the following parameters BV/TV, fractional formation surface, and fractional resting surface was found only in relation to sample 1-UL ( $P = .011$ ,  $P = .020$ , and  $P = .009$ , respectively).

The FE analysis in which occlusal loading was superimposed over the orthodontic load showed that the corresponding strains in the alveolar bone around the implant easily surpassed 400  $\mu\text{strain}$  and were therefore within the adapted window (Fig 11).

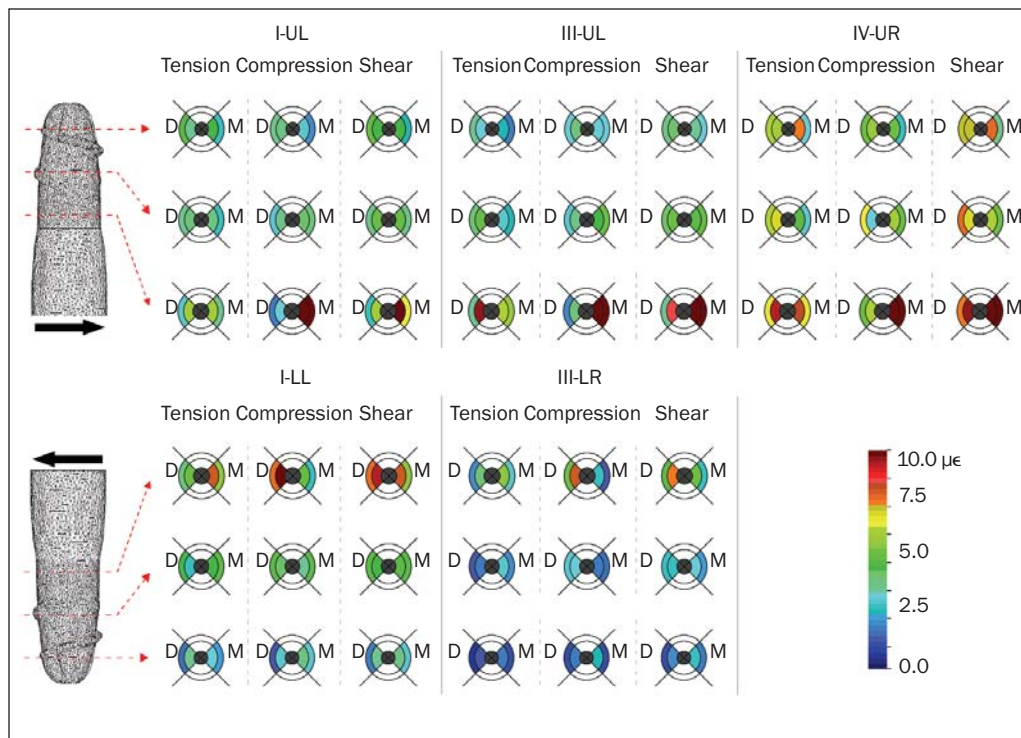


**Fig 10** Maximal compressive, tensile, and shear strains in  $\mu\epsilon$  in horizontal cross sections of the alveolar bone corresponding to the regions selected for histologic evaluation. The colors represent the strains, averaged for the region of interest, of the bone tissue alone.

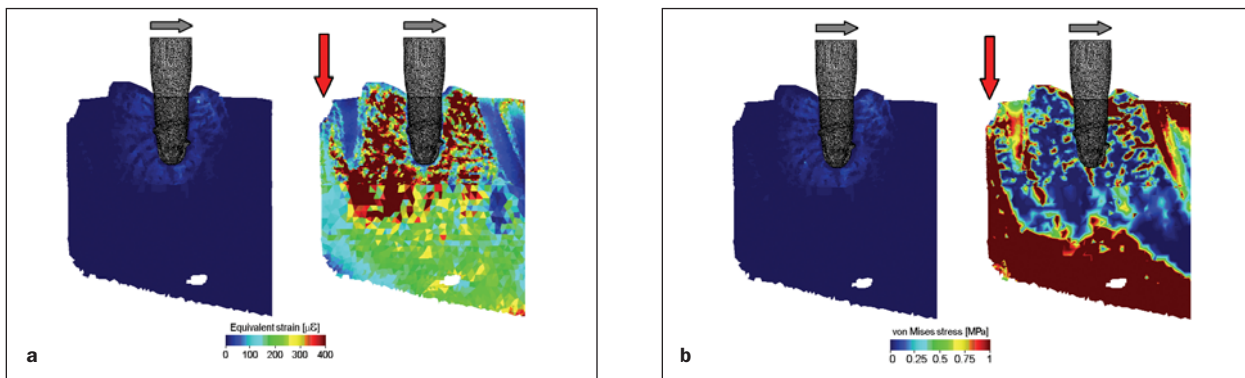


**Fig 11** Equivalent strain distributions in a vertical cross section of the alveolar bone of sample 3-LR following the application of a 50-cN orthodontic force alone (*a, left*) and the application of the same orthodontic load together with an occlusal force of 55 N at the canine-premolar region (*a, right*). Von Mises stress distribution in the same cross section before and after occlusal load application are shown in *b*. Strains are given in  $\mu\epsilon$  and MPa, respectively.

## DISCUSSION

An animal experiment was carried out on 4 male *M fascicularis* monkeys. Macaque monkeys have been used mainly in relation to experiments focusing on bone<sup>15,33–35</sup> and bone around implants.<sup>21,36–42</sup> The advantage of using monkeys instead of smaller animals is their similarity to humans with respect to function, bone morphology, and remodeling. The disadvantages are that the number of individuals that

can be included in a study is limited for both ethical and economic reasons and that larger animals are never as uniform in physiologic traits as smaller animals because the latter are generated using the inbred strain procedure.<sup>43–46</sup> This was also obvious in the present study, as monkeys 2 and 3 differed significantly from the others with respect to some of the bone-activity parameters. In this study large male monkeys were selected to ensure adequate alveolar ridge size and height for implant placement.

Microtomography as applied in the present study has become a well-established tool in the field of bone mechanics,<sup>47</sup> where it is predominantly used to reconstruct the structure of trabecular bone and, recently, to investigate peri-implant bone.<sup>48-51</sup> The enhancement of microradiographic images using a monochromatic beam compared to traditional microradiographs was described previously by Jung et al.<sup>50</sup> In the present study the  $\mu$ CT scanning technique and a monochromatic beam were combined to generate high-resolution  $\mu$ CT scan datasets free of beam artifacts. Correspondence between histologic sections and tomographic sections was recently demonstrated by Bernhardt et al<sup>52</sup>; however, in the present study, only qualitative examinations were performed.

More BIC is generally believed to generate better implant stability; however, it has been shown that the type of bone at the bone-implant interface is important as well.<sup>8,9,53</sup> From histologic evaluation of undecalcified sections, it is possible to retrieve both the amount of bone directly in contact with the implant and the type of bone present at the interface. Moreover, the histologic sectioning method is superior to  $\mu$ CT in terms of image contrast and sharpness; thus, serial sections may provide more reliable information than the  $\mu$ CT scanning technique. However, when the bone block contains a metal implant, thin sections cannot be cut. A diamond milling saw, which is typically 400  $\mu$ m thick, must be used; therefore, a significant quantity of bone is lost in the cutting process. Thus, accurate 3D reconstruction of bone segments containing implants cannot be accomplished using histologic sections.<sup>28,49</sup> This drawback was overcome by using an SR-based  $\mu$ CT-scanning technique to produce a true high-quality 3D representation of the bone structure.

The modeling process has a large influence on the results of an FE analysis. It is not possible to make predictions if the morphologic and geometric aspects are not properly described. Despite this, most previous FE models of bone with dental implants were either generated by approximating the alveolar bone to a regular geometrical shape (eg, cubic, cylindrical) and defining an arbitrarily thickness of the cortical bone or derived from serial sections of undecalcified specimens.<sup>18,21,28,54,55</sup> In the present study the 5 FE models were built from accurate 3D datasets from which both the outer shape as well as the inner morphology could be retrieved. The loading regime could thus be applied exactly as it was in the *in vivo* situation. Consequently, the results were strongly influenced by individual variations with respect to alveolar bone morphology, implant inser-

tion position, and type of bony support. This corroborated the results of Van Oosterwyck et al, who described the impact of the level of marginal bone loss on the load-transfer mechanism from the implant to the surrounding alveolar bone.<sup>29</sup> The deformation of the implant itself can be neglected, as its stiffness is orders of magnitude higher than that of the supporting bone. However, the deformation of the bone surrounding the implant is dependent on the type of movement of the implant, which, in its turn, is dependent on the quality of the bony support. An implant loaded with the same pattern of forces inserted in trabecular bone presents a substantially different type of displacement than an implant that is partly placed in cortical bone. This was particularly obvious in the cases of implants 3-LR and 3-UL, which were partially inserted into the buccal cortex. In this way most of the load was transferred through the buccal cortex and not to the trabecular bone.

In this study the interface between the bone and the implant was supposed to be fully rigid. This could be considered a limitation of the study. The significant impact of bonding conditions on the strain/stress level around a loaded implant has been described by Van Oosterwyck et al.<sup>26</sup> However, Van Oosterwyck et al also showed that when a thin layer of bone representing the lamina dura is added at the implant interface, strain concentrations at the interface are substantially reduced, and the differences in load transfer between a bonded and a free-contact interface become less marked. From the SR-based  $\mu$ CT scans, it was clear in each case that a layer of new bone had formed around the entire endosseous surface of the implant. For this reason the role of the interface condition only played a minor role in the FE model. The BIC confirmed that the implants were well osseointegrated; thus, tensile bonding between the implant surface and the surrounding bone could be hypothesized.<sup>10</sup>

The MS/BS ratio and the BV/TV ratio were found to be higher in areas subjected to compression rather than tension. This phenomenon can be explained by 2 possible scenarios. First, according to the theories of Frost, bone is more sensitive to compression than tension; this is demonstrated by the fact that bone formation occurs on the concave side of long bones and resorption on the convex side.<sup>56-58</sup> The second scenario is based on the fact that the bone-implant interface is always mediated by a thin layer (20 to 400 nm) of amorphous material.<sup>53,59,60</sup> This could generate a more compliant contact on the tension side than on the compression side, so that bone experiences higher stresses on the latter. As the present sample size was relatively small, a convincing interpretation of the present data cannot be put forward.

The strain levels calculated in the regions around the implants were substantially lower (5 to 20  $\mu$ strain) than the one prescribed by Frost for the adapted window (50 to 1,500  $\mu$ strain) and far from the mild overload window (1,500 to 3,000  $\mu$ strain).<sup>61</sup> However, from the histologic measurements it could be seen that new bone was formed around the endosseous part of the implants and that bone (re)modeling activity around the implant was actually high, although it decreased from the implant surface outward, corroborating the findings of Roberts et al<sup>17</sup> and Garetto et al.<sup>8</sup> One possible explanation could be that the strain levels proposed by Frost<sup>61,62</sup> were developed in relation to load-bearing bones and not in relation to the case of stress caused by nonfunctional loading. Another explanation is related to the loading protocol used. It has been shown that when pure static loads are applied to functionally isolated bones, bone remodeling is not affected.<sup>63</sup> However, when a static load is applied to bone in a living subject, the static load is superimposed on the one produced by functional activity. The combined load generates larger dynamic bone strain<sup>19,64</sup> than would be produced by either load acting alone. The present study indicates that when an orthodontic (static) loading regime is superimposed on a functional load, the deformation mode of the alveolar bone is affected by the overall bending of the jaw. Indeed, the resulting peri-implant strains were much higher than the ones calculated in case of the orthodontic load alone. When the strains are calculated this way, they surpass 400  $\mu$ strains; thus, they fall within the adapted window. These strains in the bone surrounding endosseous implants could be explained as the result of stress accumulation generated by the stiffness mismatch between a high-stiffness material (titanium) and a low-stiffness material (bone) when a functional load is applied.

In the present study extensive bone formation was found around both loaded and control implants. Bone formation increased slightly after orthodontic loading was superimposed on functional loading. Bone remodeling parameters decreased from the implant surface outward. This is in agreement with the results of Roberts et al<sup>17</sup> and Garetto et al.<sup>8</sup> The higher remodeling rate could act as a physiologic repairing mechanism to replace old bone and repair microcracks caused by fatigue.<sup>65</sup> The high remodeling rate could also be explained as a way to keep the bone tissue in these areas at a lower level of stiffness. This "soft bone" layer would then function as a natural shock absorber around the endosseous implants. The lower stiffness is achieved by a higher activation frequency, thereby keeping the mineralization level in the bone matrix lower than in normal

mature bone. The latter mechanism takes advantage of the 2-phase maturation process that characterizes bone matrix mineralization. During the first phase, which takes place within days of implant placement, primary mineralization occurs, and osteoblasts deposit about 70% of the mineral content found in natural mature bone. In the second phase, the remaining 30% is incorporated in the matrix by a noncellular process; this phase is a crystal growth phenomenon that occurs over a period of months.<sup>66</sup> A continuously high remodeling rate would result in the initiation of a new remodeling process before the second phase of bone mineralization could begin. These hypotheses are also corroborated by a study by Huja et al,<sup>20,67</sup> who found bone proximal to the implant surface to be more "compliant" than mature bone, thus limiting microdamage initiation.

With regard to the type and quality of bone at different sites around the endosseous parts of the implants on a more macroscopic scale, the present results are in agreement with those of Barbier and Schepers.<sup>45</sup> In a dog model they observed that the amount of bone tissue around the implants was increased toward the implant surface and that the amount of bone tissue and remodeling activity increased from the apex toward the cervical region. This may suggest primarily cortical anchorage of the implants both in the maxilla and in the mandible, similar to what was found in the mandibles of monkeys by Sahin et al.<sup>41</sup> The development of a lamina dura in contact with the implant could also be explained as an adaptive mechanism with the purpose of reducing strain levels in the trabecular bone surrounding the implant. Indeed, it is evident that the same load conditions can result in less deformation if the stiffness of the material is higher.

## CONCLUSIONS

In the present study the effect of mechanical adaptation of alveolar bone at tissue level was evaluated through a concerted approach of multiple techniques. It was anticipated that individual differences between the recipients would have a large effect on the results; therefore, case-specific models were used.<sup>68</sup> These variations were indeed found to have a significant impact on the (re)modeling dynamics and load transfer mechanisms around the implants. The magnitudes of the orthodontic forces were small relative to functional loading and consequently played only a minor role in the bone reactions around endosseous implants. The orthodontic loading of dental implants is well accepted when applied after an appropriate healing period to avoid interference

with the healing procedure. Individual reaction and variation in the anatomy of the insertion site played a greater role in the tissue reaction adjacent to the implants.

## ACKNOWLEDGMENTS

The authors acknowledge Thomas Kofod, Department of Maxillofacial Surgery, Aarhus University Hospital, Denmark, for his support in the surgical procedure; and Felix Beckmann, GKSS c/o HASYLAB at DESY, Hamburg, Germany, for his support in the  $\mu$ CT scanning of the samples. This research was partly supported by IHP-contract II-00-064 EC of the European Commission. The dental implants and the Sentalloy springs were kindly provided by Biaggini Medical Devices (La Spezia, Italy) and Scanorto (Charlottenlund, Denmark), respectively.

## REFERENCES

- Brånemark P-I, Adell R, Breine U, Hansson BO, Lindström J, Ohlsson A. Intra-osseous anchorage of dental prostheses. I. Experimental studies. *Scand J Plast Reconstr Surg* 1969;3(2): 81–100.
- Albrektsson T, Lekholm U. Osseointegration: Current state of the art. *Dent Clin North Am* 1989;33:537–554.
- Brunski JB. Biomechanical factors affecting the bone-dental implant interface. *Clin Mater* 1992;10:153–201.
- Listgarten MA, Lang NP, Schroeder HE, Schroeder A. Periodontal tissues and their counterparts around endosseous implants [corrected and republished with original paging, article originally printed in *Clin Oral Implants Res* 1991;2(1):1–19]. *Clin Oral Implants Res* 1991;2(3):1–19.
- Brånemark P-I, Hansson BO, Adell R, et al. Osseointegrated implants in the treatment of the edentulous jaw. Experience from a 10-year period. *Scan J Plast Reconstr Surg* 1977;16 (suppl):1–132.
- Roberts WE, Helm FR, Marshall KJ, Gongloff RK. Rigid endosseous implants for orthodontic and orthopedic anchorage. *Angle Orthod* 1989;59:247–256.
- Deguchi T, Takano-Yamamoto T, Kanomi R, Hartsfield JK Jr, Roberts WE, Garetto LP. The use of small titanium screws for orthodontic anchorage. *J Dent Res* 2003;82:377–381.
- Garetto LP, Chen J, Parr JA, Roberts WE. Remodeling dynamics of bone supporting rigidly fixed titanium implants: A histomorphometric comparison in four species including humans. *Implant Dent* 1995;4:235–243.
- Sennerby L, Thomsen P, Ericson LE. A morphometric and biomechanical comparison of titanium implants inserted in rabbit cortical and cancellous bone. *Int J Oral Maxillofac Implants* 1992;7:62–71.
- Skripitz R, Aspenberg P. Tensile bond between bone and titanium—A reappraisal of osseointegration. *Acta Orthop Scand* 1998;69:315–319.
- Roberts WE. Bone tissue interface. *J Dent Educ* 1988;52:804–809.
- Frost HM. Tetracycline-based histological analysis of bone remodeling. *Calcif Tissue Res* 1969;3:211–237.
- Parfitt AM, Drezner MK, Glorieux FH, et al. Bone histomorphometry: Standardization of nomenclature, symbols, and units. Report of the ASBMR Histomorphometry Nomenclature Committee. *J Bone Miner Res* 1987;2:595–610.
- Roberts WE, Smith RK, Zilberman Y, Mozsary PG, Smith RS. Osseous adaptation to continuous loading of rigid endosseous implants. *Am J Orthod* 1984;86:95–111.
- Jerome CP. Estimation of the bone mineral density variation associated with changes in turnover rate. *Calcif Tissue Int* 1989;44:406–410.
- Parfitt AM. Osteonal and hemi-osteonal remodeling: The spatial and temporal framework for signal traffic in adult human bone. *J Cell Biochem* 1994;55:273–286.
- Roberts WE, Marshall KJ, Mozsary PG. Rigid endosseous implant utilized as anchorage to protract molars and close an atrophic extraction site. *Angle Orthod* 1990;60:135–152.
- Chen J, Chen K, Garetto LP, Roberts WE. Mechanical response to functional and therapeutic loading of a retromolar endosseous implant used for orthodontic anchorage to mesially translate mandibular molars. *Implant Dent* 1995;4:246–258.
- Roberts WE. Bone physiology of tooth movement, ankylosis, and osseointegration. *Semin Orthod* 2000;6(3):173–182.
- Huja SS, Katona TR, Burr DB, Garetto LP, Roberts WE. Microdamage adjacent to endosseous implants. *Bone* 1999;25:217–222.
- Baiamonte T, Abbate MF, Pizzarello F, Lozada J, James R. The experimental verification of the efficacy of finite element modeling to dental implant systems. *J Oral Implantol* 1996;22:104–110.
- Lozada JL, Abbate MF, Pizzarello FA, James RA. Comparative three-dimensional analysis of two finite-element endosseous implant designs. *J Oral Implantol* 1994;20:315–321.
- Meyer U, Vollmer D, Runte C, Bourauel C, Joos U. Bone loading pattern around implants in average and atrophic edentulous maxillae: A finite-element analysis. *J Maxillofac Surg* 2001;29:100–105.
- Cook SD, Klawitter JJ, Weinstein AM. The influence of implant geometry on the stress distribution around dental implants. *J Biomed Mater Res* 1982;16:369–379.
- Rieger MR, Mayberry M, Brose MO. Finite element analysis of six endosseous implants. *J Prosthet Dent* 1990;63:671–676.
- Van Oosterwyck H, Duyck J, Vander SJ, et al. The influence of bone mechanical properties and implant fixation upon bone loading around oral implants. *Clin Oral Implants Res* 1998;9:407–418.
- Chen J, Esterle M, Roberts WE. Mechanical response to functional loading around the threads of retromolar endosseous implants utilized for orthodontic anchorage: Coordinated histomorphometric and finite element analysis. *Int J Oral Maxillofac Implants* 1999;14:282–289.
- Melsen B, Olesen M, Oestergaard L, Agerbaek N, Lang K. The relationship between strain values and cellular reaction studied in trabecular bone by means of a finite element analysis. In: Davidovitch Z, Norton LA (eds). *Biological Mechanics of Tooth Movements and Craniofacial Adaptation*. Boston, MA: Harvard Society for the Advancement of Orthodontics, 1996:213–221.
- Van Oosterwyck H, Vander Sloten J, Puers R, Naert I. Finite element studies on the role of mechanical loading in bone response around oral implants. *Meccanica* 2002;37:441–451.
- Gundersen HJ, Bagger P, Bendtsen TF, et al. The new stereological tools: Disector, fractionator, nucleator and point sampled intercepts and their use in pathological research and diagnosis. *APMIS* 1988;96:857–881.
- Bonse U, Busch F, Günnewig O, et al. 3D computed X-ray tomography of human cancellous bone at 8 microns spatial and 10(–4) energy resolution. *Bone Miner* 1994;25:25–38.

32. Cattaneo PM, Dalstra M, Frich LH. A three-dimensional finite element model from computed tomography data: A semi-automated method. *Proc Inst Mech Eng [H]* 2001;215:203–213.
33. Hylander WL. Mandibular function in *Galago crassicaudatus* and *Macaca fascicularis*: An in vivo approach to stress analysis of the mandible. *J Morphol* 1979;159:253–296.
34. Jerome CP, Peterson PE. Nonhuman primate models in skeletal research. *Bone* 2001;29:1–6.
35. Bouvier M, Hylander WL. The mechanical or metabolic function of secondary osteonal bone in the monkey *Macaca fascicularis*. *Arch Oral Biol* 1996;41:941–950.
36. Barzilay I, Graser GN, Iranpour B, Natiella JR, Proskin HM. Immediate implantation of pure titanium implants into extraction sockets of *Macaca fascicularis*. Part II: Histologic observations. *Int J Oral Maxillofac Implants* 1996;11:489–497.
37. Barzilay I, Graser GN, Iranpour B, Proskin HM. Immediate implantation of pure titanium implants into extraction sockets of *Macaca fascicularis*. Part I: Clinical and radiographic assessment. *Int J Oral Maxillofac Implants* 1996;11:299–310.
38. Melsen B, Costa A. Immediate loading of implants used for orthodontic anchorage. *Clin Orthod Res* 2000;3:23–28.
39. Romanos G, Toh CG, Siar CH, et al. Peri-implant bone reactions to immediately loaded implants. An experimental study in monkeys. *J Periodontol* 2001;72:506–511.
40. Wadamoto M, Akagawa Y, Sato Y, Kubo T. The three-dimensional bone interface of an osseointegrated implant. I: A morphometric evaluation in initial healing. *J Prosthet Dent* 1996;76:170–175.
41. Sahin S, Akagawa Y, Wadamoto M, Sato Y. The three-dimensional bone interface of an osseointegrated implant. II: A morphometric evaluation after three months of loading. *J Prosthet Dent* 1996;76:176–180.
42. Carr AB, Gerard DA, Larsen PE. Quantitative histomorphometric description of implant anchorage for three types of dental implants following 3 months of healing in baboons. *Int J Oral Maxillofac Implants* 1997;12:777–784.
43. Dagnaes-Hansen F. Laboratory animal genetics and genetic monitoring. In: Van Hoosier GL Jr, Hau J (eds). *Handbook of Laboratory Animal Science*, ed 2. Boca Raton, FL: CRC Press, 2003:89–124.
44. Pilon JJ, Kuijpers-Jagtman AM, Maltha JC. Magnitude of orthodontic forces and rate of bodily tooth movement. An experimental study. *Am J Orthod Dentofacial Orthop* 1996;110:16–23.
45. Barbier L, Schepers E. Adaptive bone remodeling around oral implants under axial and nonaxial loading conditions in the dog mandible. *Int J Oral Maxillofac Implants* 1997;12:215–223.
46. Gotfredsen K, Rostrup E, Hjorting-Hansen E, Stoltze K, Budtz-Jorgensen E. Histological and histomorphometrical evaluation of tissue reactions adjacent to endosteal implants in monkeys. *Clin Oral Implants Res* 1991;2:30–37.
47. Müller R, Rügsegger P. Micro-tomographic imaging for the nondestructive evaluation of trabecular bone architecture. *Stud Health Technol Inform* 1997;4061–4079.
48. Kiba H, Hayakawa T, Oba S, Kuwabara M, Habata I, Yamamoto H. Potential application of high-resolution microfocus x-ray techniques for observation of bone structure and bone-implant interface. *Int J Oral Maxillofac Implants* 2003;18:279–285.
49. Sennerby L, Wennerberg A, Pasop F. A new microtomographic technique for non-invasive evaluation of the bone structure around implants. *Clin Oral Implants Res* 2001;12:91–94.
50. Jung H, Kim HJ, Hong S, et al. Osseointegration assessment of dental implants using a synchrotron radiation imaging technique: A preliminary study. *Int J Oral Maxillofac Implants* 2003;18:121–126.
51. Yip G, Schneider P, Roberts EW. Micro-computed tomography: High resolution imaging of bone and implants in three dimensions. *Semin Orthod* 2004;10:174–187.
52. Bernhardt R, Scharnweber D, Müller B, et al. Comparison of microfocus- and synchrotron x-ray tomography for the analysis of osteointegration around Ti6Al4V implants. *Eur Cell Mater* 2004;742–751.
53. Sennerby L, Ericson LE, Thomsen P, Lekholm U, Astrand P. Structure of the bone-titanium interface in retrieved clinical oral implants. *Clin Oral Implants Res* 1991;2:103–111.
54. Pierrisnard L, Hure G, Barquins M, Chappard D. Two dental implants designed for immediate loading: A finite element analysis. *Int J Oral Maxillofac Implants* 2002;17:353–362.
55. Qin YX, McLeod KJ, Guilak F, Chiang FP, Rubin CT. Correlation of bony ingrowth to the distribution of stress and strain parameters surrounding a porous-coated implant. *J Orthop Res* 1996;14:862–870.
56. Frost HM. Skeletal structural adaptations to mechanical usage (SATMU): 1. Redefining Wolff's law: The bone modeling problem. *Anat Rec* 1990;226:403–413.
57. Frost HM. Wolff's Law and bone's structural adaptations to mechanical usage: An overview for clinicians. *Angle Orthod* 1994;64:175–188.
58. Frost HM. Some ABC's of skeletal pathophysiology. 6. The growth/modeling/remodeling distinction. *Calcif Tissue Int* 1991;49:301–302.
59. Albrektsson T, Zarb G, Worthington P, Eriksson AR. The long-term efficacy of currently used dental implants: A review and proposed criteria of success. *Int J Oral Maxillofac Implants* 1986;1:11–25.
60. Linder L, Albrektsson T, Brånemark P-I, et al. Electron microscopic analysis of the bone-titanium interface. *Acta Orthop Scand* 1983;54:45–52.
61. Frost HM. Skeletal structural adaptations to mechanical usage (SATMU): 2. Redefining Wolff's law: The remodeling problem. *Anat Rec* 1990;226:414–422.
62. Frost HM. Bone's mechanostat: A 2003 update. *Anat Rec Discov Mol Cell Evol Biol* 2003;275A:1081–1101.
63. Lanyon LE, Rubin CT. Static vs dynamic loads as an influence on bone remodelling. *J Biomech* 1984;17:897–905.
64. Trisi P, Rebaudi A. Progressive bone adaptation of titanium implants during and after orthodontic load in humans. *Int J Periodontics Restorative Dent* 2002;22:31–43.
65. Verna C, Dalstra M, Lee TC, Cattaneo PM, Melsen B. Microcracks in the alveolar bone following orthodontic tooth movement: A morphological and morphometric study. *Eur J Orthod* 2004;26:459–467.
66. Marotti G, Favia A, Zallone AZ. Quantitative analysis on the rate of secondary bone mineralization. *Calcif Tissue Res* 1972;10:67–81.
67. Huja SS, Katona TR, Moore BK, Roberts WE. Microhardness and anisotropy of the vital osseous interface and endosseous implant supporting bone. *J Orthop Res* 1998;16:54–60.
68. Baumrind S. Taking stock: A critical perspective on contemporary orthodontics. *Orthod Craniofac Res* 2004;7:150–156.